Renewable Energy 236 (2024) 121381

Contents lists available at ScienceDirect

Renewable Energy

journal homepage: www.elsevier.com/locate/renene

Objective representative flow field selection for tidal array layout design

Connor Jordan [*], Joseba Agirre, Athanasios Angeloudis

School of Engineering, Institute for Infrastructure and the Environment, University of Edinburgh, Edinburgh, UK

ARTICLE INFO

Keywords:
Optimisation
Flow field selection
Tidal energy
Tidal array

ABSTRACT

The representation of flow across influential spatiotemporal scales introduces a challenge when micro-siting tidal stream turbine arrays. Robust representative approximations could accelerate design optimisation, yet there is no consensus on what defines the most appropriate flow conditions. We summarise existing approaches to representative flow field selection for array optimisation and propose an objective-driven process. The method curates a subset of flow fields that best captures relevant dynamics, enabling the streamlined representation of tidal cycles. To demonstrate the method, we consider flow modelling data in the Inner Sound of the Pentland Firth, Scotland, UK. We examine the impact of flow field inputs to array design through comparative analyses using a heuristic array optimisation process. Results indicate notable sensitivity of the turbine layout to the flow conditions selected. For the case study presented, our method led to 4%–5% energy yield prediction improvements relative to use of simple time-interval based approaches and up to 2% improvement against using peak flow fields; these can be pivotal margins to secure feasibility by developers. We also find that using the data associated with a single monitored point across the array for flow field selection can lead to sub-optimal results, emphasising the need for accurate spatiotemporal representation.

1. Introduction

Oceanic currents are influenced by various processes, ranging from planetary-scale interactions and tidal movements to localised changes in temperature, salinity, and wind stress. This gives rise to highly variable spatial flow patterns, especially in shallow waters with rugged coastlines and bed topography (e.g. Polagye and Thomson [1]). Conversely, temporal predictability is often cited as a major attribute of tidal energy, allowing long-term resource forecasting through harmonic analysis [2,3]. Over shorter duration, true flow behaviour cannot be predicted by harmonics, and more sophisticated approaches are required to consider the impact of waves and wind [4]. On spatial variability, Warder et al. [5] demonstrate the presence of non-deterministic effects by forcing a regional hydrodynamics model with only a single constituent (M2, principal lunar semi-diurnal) and presenting the departure from purely periodic behaviour within a highly energetic tidal site. The spatial variation in temporal patterns across marine sites necessitates hydrodynamic modelling for forecasting at less surveyed sites. The complex non-linearity is only further exacerbated by the introduction of infrastructure such as dams, ports, turbines, coastal defence systems and maritime traffic.

Engineers must consider these spatio-temporal flow dynamics in both design and operation activities. For tidal range power plants, Pappas et al. [6] found that the average potential energy of a tidal range site can vary by up to 30% depending on which 28-day tidal cycle was used in a resource assessment. Similarly, tidal stream turbine arrays are intrinsically linked to the spatio-temporal variability of tidal flows, as the energy output is contingent upon the diverse flow patterns exhibited across the array site. Several studies discuss the influence of tidal asymmetry [7,8] and tidal resource variability in high energy regions, even deeming some sites infeasible for tidal energy deployment [9].

Considering the technical implications, it becomes essential that flow characteristics are reliably resolved when modelling a marine site. Typically, this is achieved through a calibration exercise, following which a model might be used for environmental impact assessment, forecasting or energy yield predictions. In such assessments, model run-time is a balance of computational burden and satisfactory representation of the hydrodynamics. For some tasks, such as pollutant tracking and sediment transport, the intricacies of flow dynamics require transient modelling over extended periods of time. As climate change impacts increasingly influence coastal and marine environments, simulations may even span decades [10]. For applications such as tidal array optimisation, opportunities exist to leverage the cyclic nature of tidal flows. By focusing on specific tidal phases or cycles, we can hypothesise that computations can be accelerated without compromising the objective's accuracy.

Avoiding sub-optimal investigations whilst using a subset of flow data, requires careful consideration and judgement in the selection of

---

[*] Corresponding author.
E-mail address: C.Jordan@ed.ac.uk (C. Jordan).

https://doi.org/10.1016/j.renene.2024.121381
Received 12 March 2024; Received in revised form 17 July 2024; Accepted 15 September 2024

instantaneous fields or tidal cycles for analyses. This is the challenge we seek to address. We devise a statistical objective-focussed approach to provide a reduced representation of the transient tidal flow. We subsequently compare methods for reduced cost flow representation in the context of tidal array optimisation.

2. Background

Gunn and Stock-Williams [11] comment on model calibration decisions, emphasising the need for selective validation parameters to suit the objective of interest. Following validation, a hydrodynamic model should provide a quantifiable degree of confidence, given known limitations. However, when applying a calibrated model for subsequent purposes, there is a risk of sub-optimal utilisation. Table 1 summarises examples specific to tidal stream array optimisation. Some of the studies focus solely on methodology development that rely on idealised domains, others apply calibrated hydrodynamic models in practical scenarios in the optimisation process. Funke et al. [12] and Culley et al. [13] calculate the optimisation gradient using an adjoint-based approach which is known for being memory intensive. The calculation of the adjoint is attractive as it enables partial differential equation (PDE) constrained gradient evaluations that can inform the optimisation. However, in order to balance the need for device-scale resolution and the method's memory requirements, steady state cases were used to minimise computational burden [14]. For practical cases, these approaches must be extended to account for transient tidal flows and realistic turbine characteristics. Within their exploration of economic constrained optimisation, Goss et al. [15] forced their model using the principal M2 constituent, consequently overlooking monthly and annual variations. Funke et al. [16] and Zhang et al. [17] extended the application of the adjoint-optimisation methodology to incorporate realistic tidal forcing and bathymetry survey data, providing realistic variation both temporally and spatially. However, in all unsteady applications of adjoint based optimisation, a non-discrete representation of the array using mesh resolution exceeding the turbine diameter was imposed. This 'continuous' representation involves representing the entire array as one smeared momentum sink, rather than modelling turbines independently. This makes it challenging to consider finer scale practical constraints such as those regarding the support structure foundation and individual turbine wake evolution. Additional refinement in resolution can be applied to address this issue, at considerable computational expense.

Surrogate models can reduce computational cost, circumventing the use of PDE-constrained optimisation. This provides substantially more rapid optimisation in practical cases while sacrificing some of the local and array blockage considerations in the micrositing process, as discussed in [25]. As it would be memory-consuming to store all the flow fields to superimpose wakes onto, the optimisation makes use of fewer instantaneous flow fields. The optimisation objective is formulated as power maximisation, or variants related to this. Optimisation is even more constrained if performed in 3D models. For example, González-Gorbeña et al. [23] used a single steady-state simulation for both ebb and flood conditions to make predictions on optimal array structure. Lo Brutto et al. [21] and Mubarok et al. [27] use frequency of principal direction and average velocity magnitude, determined from the hydrodynamic model, to generate a "tidal rose". The flow fields are simplified to a series of uniform flows and thus all spatial variation across each flow field is lost. This would therefore only apply for very small arrays and a uniform basin geometry. Another route has been the use of a greedy based technique directly within the hydrodynamic model, such as in [29]. There, each turbine was introduced based on full flood-ebb cycles and the entire simulation re-run after each placement.

To our knowledge, no study so far (e.g. Table 1) simultaneously combines a realistic turbine power curve, non-linear spatial representation and transient flow in the optimisation process. In Jordan et al. [26], a simple experiment of artificially over-estimating the velocity magnitude for the flow fields used in optimisation was conducted. This determined that the resultant array power improved up until an optimal point, governed in part by the rated speed. This links back to several key factors related to the efficiency of a tidal turbine array, most importantly balancing the ratio of wake interaction versus array density at high energy regions. This is in turn related to the cut-in, rated and cut-out speeds of the turbines and the corresponding ratio of flow speeds above and below these thresholds. Individual turbine and array performance can also be substantially impacted by local, array and global blockage effects. Identifying a satisfactory representation of the flow that ensures an accurate balance between wake interaction versus array density at high energy regions motivates the development of optimal flow field selection strategies.

3. Methodology

Various array layout optimisation approaches could be used to investigate the influence of the flow fields or cycles used for design, however the methodology developed in [25] is deployed for its low computational cost. This is described in Section 3.1. The hypothesised impact of the flow field selection methodology for other array design methods can be found in the appendices. The proposed methodology for flow field selection is then described in Section 3.2 and the setting for its application, as well as investigation of other methods, is described in Section 3.3.

3.1. Array design

3.1.1. Resource modelling

Thetis[1] [30] is employed for hydrodynamic modelling, utilising *Firedrake* [31] to solve associated partial differential equations using the finite element method. *Thetis* is applied in its 2D configuration, solving the non-conservative form of the non-linear shallow-water equations,

$$\frac{\partial \eta}{\partial t} + \nabla \cdot (H_d \mathbf{u}) = 0, \tag{1}$$

$$\frac{\partial \mathbf{u}}{\partial t} + \mathbf{u} \cdot \nabla \mathbf{u} + g \nabla \eta = \nabla \cdot (\nu (\nabla \mathbf{u} + \nabla \mathbf{u}^T)) - \frac{\boldsymbol{\tau_b}}{\rho H_d} - \frac{c_t}{\rho H} |\mathbf{u}| \mathbf{u} + f \mathbf{u}^{\perp}, \tag{2}$$

where η is the water elevation, H_d is the total water depth, $\mathbf{u}$ is the depth-averaged velocity vector, and ν is the kinematic viscosity of the fluid. The term $f\mathbf{u}^{\perp}$ represents the Coriolis "force", $\mathbf{u}^{\perp}$ is the velocity vector rotated counter-clockwise over 90°, and $f = 2\Omega \sin(\zeta)$ with Ω the angular frequency of the Earth's rotation and ζ the latitude. The bed shear stress ($\boldsymbol{\tau_b}$) is represented through the Manning's n_M formulation as per [32]:

$$\frac{\boldsymbol{\tau_b}}{\rho} = g n_M^2 \frac{|\mathbf{u}|\mathbf{u}}{H_d^{\frac{1}{3}}}, \tag{3}$$

The treatment of inter-tidal processes, discretisation and time-marching are applied consistently to Jordan et al. [25]. The force on the tidal array according to the linear momentum actuator disc theory is:

$$F_{\text{array}} = \frac{1}{2} \int_{\alpha} \rho \, c_t(\mathbf{x}) \, |\mathbf{u}(\mathbf{x})| \, \mathbf{u}(\mathbf{x}) \, \mathrm{d}\mathbf{x}, \tag{4}$$

where $\boldsymbol{\alpha}$ is the area of interest where the array is situated i.e. the domain over which the integral is evaluated. We define here $m = (x, y)$, such that $\mathbf{x}$ contains all pairs of coordinates m in the field. The thrust coefficient, $c_t(\mathbf{x})$, is defined as:

$$c_t(\mathbf{x}) = \left(C_t(\mathbf{u}(\mathbf{x})) \, A_t + C_{sup} A_{sup} \right) \, d(\mathbf{x}), \tag{5}$$

where A_t is the turbine swept area, C_t is the thrust coefficient as a function of the velocity $\mathbf{u}(\mathbf{x})$, and $d(\mathbf{x})$ is the local turbine density [25].

---

[1] http://thetisproject.org/

Table 1
Tidal array optimisation studies in the literature, emphasising realistic cases where available.

Ref.	Optimisation strategy	Setting	Optimisation objective	Turbine representation	Spatial variability	Temporal variability	Flow fields for optimisation	Power curve
Funke et al. [12]	Adjoint + SLSQP[a]	Inner Sound, Pentland Firth	Power	Discrete	Constant bathymetry	Steady state	1×	No
Culley et al. [13]	Adjoint + SLSQP & GA	Inner Sound, Pentland Firth	LCOE (cabling only)	Discrete	Constant bathymetry	Steady state	1×	No
Funke et al. [16]	Adjoint + L-BFGS-B	Pentland Firth	LCOE	Continuous	Full	Transient, (M_2, S_2, …)	12.5h tidal cycle	No
du Feu et al. [18]	Adjoint + SLSQP	Inner Sound, Pentland Firth	Power & Environmental Impact	Discrete	Constant bathymetry	Steady state	Peak (1×)	No
du Feu et al. [19]	Adjoint + SLSQP	Pentland Firth	LCOE & Environmental Impact	Continuous	Full	Steady state	Peak (1×)	No
Goss et al. [15]	Adjoint + L-BFGS-B	Idealised headland	LCOE	Continuous	Constant bathymetry at site	Transient, M2 forcing only	3 M2 cycles	Yes
Zhang et al. [17]	Adjoint + L-BFGS-B	Zhoushan Islands	Energy	Continuous	Full	Transient, (M_2, S_2, …)	12.42h tidal cycle	No
Zhang et al. [20]	Adjoint + SLSQP	Idealised regular channel	Power (Yaw Angle)	Discrete	None	Steady state	1×	No
Lo Brutto et al. [21]	Surrogate + PSO	Idealised	LCOE	Discrete (structured)	None	Based on tidal rose	Based on tidal rose (153×)	Yes
González-Gorbeña et al. [22]	Surrogate + enumeration	Idealised irregular channel	LCOE	Discrete (structured)	Constant bathymetry	Steady state	Sub-rated (1×)	Yes
González-Gorbeña et al. [23]	Surrogate + enumeration	Idealised regular channel	LCOE	Discrete (structured)	None	Steady state, ebb and flood	Sub-rated (2×)	Yes
Wu et al. [24]	Surrogate + DPSO	Zhoushan Islands	Energy	Discrete (structured)	Constant bathymetry	Steady state, ebb and flood	Peaks (2×)	Yes
Jordan et al. [25]	Surrogate + greedy	Inner Sound, Pentland Firth	Power (& Wake Interaction)	Discrete	Full	Transient, (M_2, S_2, …)	Neap, intermediate and spring instantaneous fields (18×)	Yes
Jordan et al. [26]	Surrogate + greedy	Inner Sound, Pentland Firth	Average Power (& Wake Interaction)	Discrete	Full	Transient, (M_2, S_2, …)	Rated (4×)	Yes
Mubarok et al. [27]	Surrogate + PSO	Idealised	LCOE	Discrete	None	Based on tidal rose	Based on tidal rose (18×)	Yes
Divett et al. [28]	Enumeration	Idealised regular channel	Power (turbine drag coefficient)	Discrete (structured)	None	Transient	1 flood/ebb cycle	N/A
Phoenix and Nash [29]	Greedy	Shannon Estuary	Energy (& Environmental Impact)	Discrete	Full	Transient (spring cycles)	Flood/ebb cycle	No

[a] SLSQP allows for more general inequality constraints, so is typically used for e.g. minimum separation constraints. L-BFGS-B is therefore typically used for continuous array representation and SLSQP for discrete.

A_{sup} represents the cross-sectional support structure area with a corresponding drag coefficient of C_{sup}. Following notation of (4), the power extracted at any given moment by the array can be approximated as

$$P_{\text{array}} = \frac{1}{2}\int \rho\, c_p(\mathbf{x})\, |\mathbf{u}(\mathbf{x})|^3\, \mathrm{d}\mathbf{x}, \tag{6}$$

where $c_p(\mathbf{x})$ is a power coefficient function given as

$$c_p(\mathbf{x}) = C_p(\mathbf{u}(\mathbf{x}))A_t d(\mathbf{x}), \tag{7}$$

and C_p is a power coefficient as per [25]. The turbine specification for this study is discussed in Section 3.3 and the thrust and power curves are plotted in Fig. 2. Finally, the concentration of the thrust at a turbine location can affect Linear Momentum Actuator Disc Theory calculation. A correction relating free-stream and through-turbine velocities is therefore applied as per Kramer and Piggott [33].

3.1.2. Layout optimisation

Surrogate modelling is applied for array design. The ambient flow fields are generated in *Thetis*. Relevant flow fields or cycles are then used as input for an analytical wake model, *FLORIS*,[2] which superimposes the predicted wake structure for each turbine when placed by the array design algorithm. The iterative algorithm introduced in [25] is used, which is described in detail in Appendix A. At each iteration, the turbine is placed in the location of highest energy, constrained by performance conditions (applied to all turbines). These constraints can be expressed mathematically, for acceptance, as:

- Minimum turbine capacity factor, $A_{\text{min}} \leq A = \min\left\{\frac{P_{\text{i}}}{P_{\text{rated}}} \mid i \in n\right\}$, where n is the number of turbines.
- Maximum reduction of power to any other turbine, $B_{\text{max}} \geq B = \max\left\{\frac{P_i^{(n-1)} - P_i^{(n)}}{P_i^{(n-1)}} \mid i \in n\right\}$ i.e. the relative change in power of each turbine in the array as a result of introducing the new turbine.
- Maximum reduction of the sum of powers of individual turbines of $\Gamma_{\text{max}} \geq \Gamma = \sum_{i=1}^{n}\left(\frac{P_i^{(n-1)} - P_i^{(n)}}{P_i^{(n-1)}}\right)$.

It should be noted that by preventing excessive wake interactions, the constraint, B, is also expected to reduce fatigue loading and in turn, prevent greater geotechnical and structural requirements. In the current implementation, performance metrics are first calculated for each flow field, then averaged and hence no specific flow field dominates the acceptance or rejection of a location for turbine deployment. The parameter values used in this study are later defined in Section 3.3.

We use the Bastankhah and Porté-Agel [34] Gaussian wake model calibrated with the turbine support structure included, as described in detail in Appendix B. The *optimisation objective* within *FLORIS* being

---

[2] https://github.com/NREL/floris

maximised can be expressed as:

$$\overline{P}_{\text{array},FLORIS} = \frac{1}{N}\sum_{i=0}^{N} w(t_i) \times P_{\text{array},FLORIS}(t_i), \tag{8}$$

subject to any constraints applied on the optimisation. N is the number of flow fields and t_i indicates the timestamp of the flow field being assessed. w is an optional weight, should certain flow fields be considered more important.

As *FLORIS* is a surrogate model, it is not appropriate for the final quantification of array yield. The final performance of the array is finally quantified in *Thetis* to make comparisons between the various arrays designed.

3.2. Flow field selection through the objective binning approach

For flow field selection, we propose Algorithm 1 to form an "objective binning" (OB) method to identify representative flow conditions. Firstly, we discuss the term 'objective' in this context. Considering array design, the *optimisation objective* is to maximise energy yield, which may be paired with other constraints such as cabling length [13] or environmental impact [18,19]. Energy yield, can equivalently be considered as the average power:

$$\overline{P}_{\text{array}} = \frac{1}{t_s}\int_{t_0}^{t_f} P_{\text{array}}\,\mathrm{d}\mathbf{t}, \tag{9}$$

where t_s is the duration of the time period simulation, given by the initial and finish time, $t_s = t_f - t_0$. For flow field selection there is no inclusion of turbines in the initial runs, therefore we require the ambient equivalent of the *optimisation objective*. We define this as the flow field selection *objective function*, $\mathcal{O}$:

$$\mathcal{O}(m,t) = \frac{1}{2}\rho\, C_p(\mathbf{u}(m,t))\, A_t\, |\mathbf{u}(m,t)|^3\,, \tag{10}$$

at a point of interest, m, at time, t. Unlike $\overline{P}_{\text{array}}$, $\mathcal{O}$ is not associated with an array density, nor averaged temporally, since we need to distinguish between fields.

Algorithm 1 firstly extracts velocity fields at the area of interest, $\boldsymbol{\alpha}$, and decomposes these to magnitude and direction. The principle flow directions allow classification into ebb and flood fields, so that the primary directional variability is preserved for optimisation. The ambient power yield, $\mathcal{O}$, is calculated across the flow field for every entry in the time series, $\mathbf{t}$. This ambient power yield is spatially averaged to form $\mathcal{O}_{\text{avg}}$, i.e.

$$\mathcal{O}_{\text{avg}}(t) = \frac{1}{A_{\boldsymbol{\alpha}}}\int_{\boldsymbol{\alpha}} \mathcal{O}(\mathbf{x},t)\,\mathrm{d}\mathbf{x}. \tag{11}$$

Ebb and flood fields are then ordered based on $\mathcal{O}_{\text{avg}}$ and binned into N_{ebb} and N_{flood} bins. Each bin is assigned a weight, w, based on the bin energy relative to the total energy over the simulation time, t_s. This weighting is required to make corrections for any energy imbalance between flood and ebb, given how the cycle energy may not perfectly divide into N equal energy groups. For example, when N is small, an equal number of flood and ebb fields will be used, despite the fact that there could be more energy in either the ebb or the flood tide. Within each bin, we define as the representative flow field, $\mathbf{u}_\alpha(\mathbf{x},t)$, that with the $\mathcal{O}_{\text{avg}}$ closest to the average bin value. Accumulating the representative flow field from each bin gives the final subset of flow fields to use from Algorithm 1.

In assessing how energetic the subset of flow fields selected are, we introduce a *yield representation index*, YRI, balancing the full cycle average ambient energy yield relative to the average ambient energy yield captured by the optimisation:

$$\text{YRI} = \frac{\frac{1}{t_s}\int_{t_0}^{t_f} \mathcal{O}_{\text{avg}}\,\mathrm{d}\mathbf{t}}{\frac{1}{N}\sum^{N}\mathcal{O}_{\text{avg}}}, \tag{12}$$

where the objective function, $\mathcal{O}_{avg}$, is the average ambient field potential power yield across the deployment region. The smaller this value, the more energetic the fields used in the optimisation are relative to the average power of the cycle used for instantaneous flow field or sub-cycle selection.

Algorithm 1 Objective-binning (OB) approach for representative flow field ($\mathbf{u}_\alpha(\mathbf{x},t)$) selection from a time series, also returning weight factors, w, subject to an objective function, $\mathcal{O}$.

```
$INPUTS$: Target number of representative fields ($N$) and model start ($t_0$) and finish time ($t_f$).
$DEFINITIONS$:
$\mathbf{u}_\alpha(\mathbf{x},\mathbf{t})$: flow velocity vector field within area of interest, $\boldsymbol{\alpha}$, over the time series, $\mathbf{t}$
$\theta_\alpha(\mathbf{x},\mathbf{t})$: flow direction field within area of interest, $\boldsymbol{\alpha}$, over the time series, $\mathbf{t}$
$\mathcal{O}_{\text{avg}}(t)$: objective function value averaged across area of interest, $\boldsymbol{\alpha}$, at time $t$
$t_i$: timestamp of representative flow field for bin $i$
$w(t_i)$: weight factor for flow field $\mathbf{u}(\boldsymbol{\alpha},t_i)$ relative to $\mathcal{O}$
Run hydrodynamic model to derive $\mathbf{u}_\alpha(\mathbf{x},\mathbf{t})$
Determine $\theta_\alpha(\mathbf{x},\mathbf{t})$ and $\mathcal{O}_\alpha(\mathbf{x},\mathbf{t})$
Determine principal flow directions, $\theta_{\text{ebb}}$, $\theta_{\text{flood}}$
Classify flow fields, $\mathbf{u}_\alpha(\mathbf{x},\mathbf{t})$, into $\mathbf{u}_{\boldsymbol{\alpha}}(\mathbf{x},\mathbf{t}_{\text{ebb}}), \mathbf{u}_{\boldsymbol{\alpha}}(\mathbf{x},\mathbf{t}_{\text{flood}})$ using $\theta_{\text{ebb}}$, $\theta_{\text{flood}}$
Spatially average objective function, $\mathcal{O}_{\text{avg}}(\mathbf{t}) = \frac{1}{A_\alpha}\sum^{\alpha}\mathcal{O}_\alpha(\mathbf{x},\mathbf{t})$
Find the total value of the objective function over the time series, $\mathcal{O}_{\text{avg,total}} = \sum^{\mathbf{t}}\mathcal{O}_{\text{avg}}(t)$
Find the total value of objective function for ebb, $\mathcal{O}_{\text{avg,ebb}} = \sum^{\mathbf{t}_{ebb}}\mathcal{O}_{\text{avg}}(t)$
Determine number of bins for each tide, $N_{\text{ebb}} = \frac{\mathcal{O}_{\text{avg,ebb}}}{\mathcal{O}_{\text{avg,total}}}\times N$, $N_{\text{flood}} = N - N_{\text{ebb}}$
Sort $\mathbf{u}_{\boldsymbol{\alpha}}(\mathbf{x},\mathbf{t}_{\text{ebb}})$, $\mathbf{u}_{\boldsymbol{\alpha}}(\mathbf{x},\mathbf{t}_{\text{flood}})$ in descending order of $\mathcal{O}_{\text{avg}}$, denoted $\mathbf{t}'_{\text{ebb}}, \mathbf{t}'_{\text{flood}}$
for tide in [ebb, flood] do
    Determine ideal bin objective function total, $\mathcal{O}_{\text{avg,ideal}} = \frac{\mathcal{O}_{\text{avg,tide}}}{N_{tide}}$
    Initiate counter and list for keeping bin timestamps, $i = 1, \mathbf{t}_{\text{bin}} = [\,[\,]$ for $i$ in range$(N_{\text{tide}})]$
    for $t_k$ in $\mathbf{t}'_{\text{tide}}$ do
        Add flow field timestamp to the $\text{bin}_\text{i}$ corresponding timestamp list, append $t_k$ to $\mathbf{t}_{bin,i}$
        Add $\mathcal{O}_{\text{avg}}$ of flow field to the bin total, $\text{bin}_\text{i} \mathrel{+}= \mathcal{O}_{\text{avg}}(t_k)$
        if $\text{bin}_\text{i} \geq \mathcal{O}_{\text{avg,ideal}}$ then
            $i \mathrel{+}= 1$, i.e. start new bin once current bin total has reached $\mathcal{O}_{\text{avg,ideal}}$
        end if
    end for
    for $i$ in range$(N_{\text{tide}})$ do
        Determine the average value of objective function for each bin, $\mathcal{O}_{\text{avg,bin}_\text{i}} = \frac{\text{bin}_\text{i}}{\text{len}(\mathbf{t}_{\text{bin,i}})}$
        Find representative time, $t_i = \arg\min_{t_k}\left(\left|\mathcal{O}_{\text{avg}}(t_k) - \mathcal{O}_{\text{avg,bin}_\text{i}}\right|\right)$ for $k$ in len$(\mathbf{t}_{\text{bin,i}})$
        Determine timestamp weight factor, $w(t_i) = \frac{\sum\mathcal{O}_{\text{bin,i}}}{\mathcal{O}_{\text{avg,total}}}$
    end for
end for
```

3.3. Case study — Inner Sound, Pentland Firth

3.3.1. Site overview

The Inner Sound of the Pentland Firth in Scotland is home to the MeyGen project, a tidal stream site currently including four operational

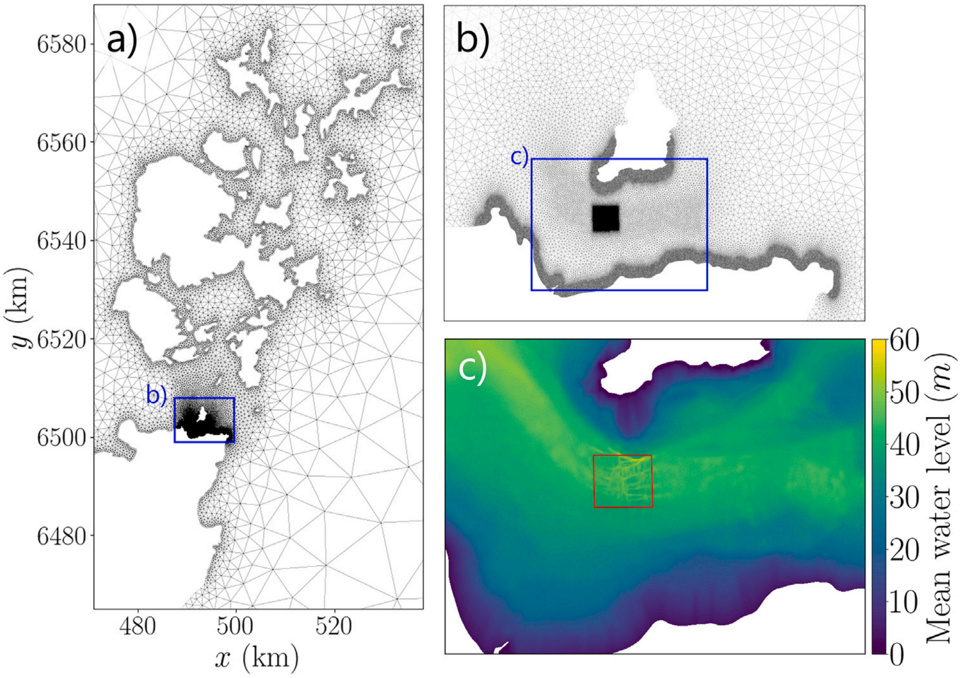

Fig. 1. Site location, (a, b) computational mesh showing Orkney isles and mainland Scotland, (c) bathymetry interpolated onto the mesh. The deployment region for optimisation is outlined in red.

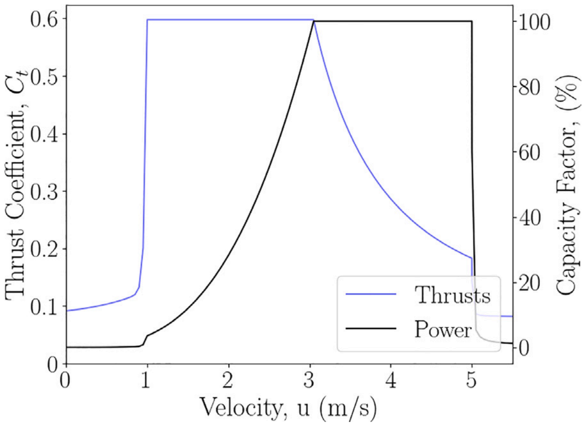

Fig. 2. Estimated thrust and power (expressed as capacity factor) curves for a SIMEC Atlantis Energy AR2000 turbine, including support structure contribution. The curves ramp up and down just prior to cut-in and post cut-out speed for model stability.

1.5 MW turbines. It is one of the several sites where UK government funding has been announced for further development [35], which sets it on-track to deliver a ≈ 50 MW array for the next instalment. Multi-faceted large-scale optimisation over varying conditions and constraints will need to be performed at sites such as MeyGen, which exhibit irregular geometry (Fig. 1b,c). It becomes critical to understand how spatio-temporal variations impact optimisation at these sites. To demonstrate the flow field selection methodology we use the Inner Sound as a case study, performing optimisation for 43×2 MW turbines (≈ 86 MW, the initial Phase '1B' target set by MeyGen) in the deployment region shown in Fig. 1c. This is the same region as used for Jordan et al. [25], where model calibration results are also presented. As in [26], support structure values of $A_{sup} = 36.4m^2$ and $C_{sup} = 0.7$ are used.

The refined mesh of Jordan et al. [26] (Fig. 1) is implemented. The element size varies from 300 m to 1500 m close to islands and the shoreline up to 20 000 m at the seaward boundaries. At the MeyGen site, the nearby coastlines are resolved to 20 m and within the deployment area, the minimum element size is 5 m on average, corresponding to $\approx \frac{1}{2}$ blade length. Further resolution would be important to capture finer turbulent structures, however demonstration of the flow field selection methodology does not require such model fidelity. Variable friction representation through the Manning's coefficient is used in the same manner as Mackie et al. [32]. Bathymetry obtained through the MeyGen project, Edina Digimap Service [36] and GEBCO[3] is used. Tidal open boundaries are forced by the Q1, O1, P1, K1, N2, M2, S2 & K2 tidal constituents from the TPXO database [37] and the model is spun up for 2 days of simulation time. The model is sequentially run over a 28 day period without turbines to subsequently provide ambient flow fields for the flow selection methodology.

3.3.2. Flow field selection for optimisation

We perform optimisation using several existing flow field selection methods reported in previous optimisation approaches (Table 3). For investigation of intuitive (i.e. empirical) methods, flow fields are selected by taking N fields at equal time intervals (EI) from representative flood and ebb cycles. The same approach but excluding slack flow fields (IS) ($|\mathbf{u}_{avg}| < 1$ m/s = cut-in speed, see Fig. 2) follows this, as in [25]. Intuitively, this reframes focus from the ambient resource to the power yield from deployed devices. This is performed with a varying number of instantaneous flow fields (6, 18, 36) from one ebb and one flood cycle, but also with twelve fields selected from three ebb and three flood cycles (3 × 12). We then proceed to investigate methods used in surrogate model approaches for flow field selection, where the number of flow fields is typically reduced to contain computational complexity. Both peak flow fields (P, [24]), and flow fields with speeds just above and below rated (R, [26]) are used separately, and then combined (PR). In all cases, the representative flood and ebb cycles are selected by adapting Algorithm 1 for use with cycles. Typically the cycle used for optimisation is chosen arbitrarily or based on major constituents (e.g. M2).

---

[3] https://www.gebco.net/

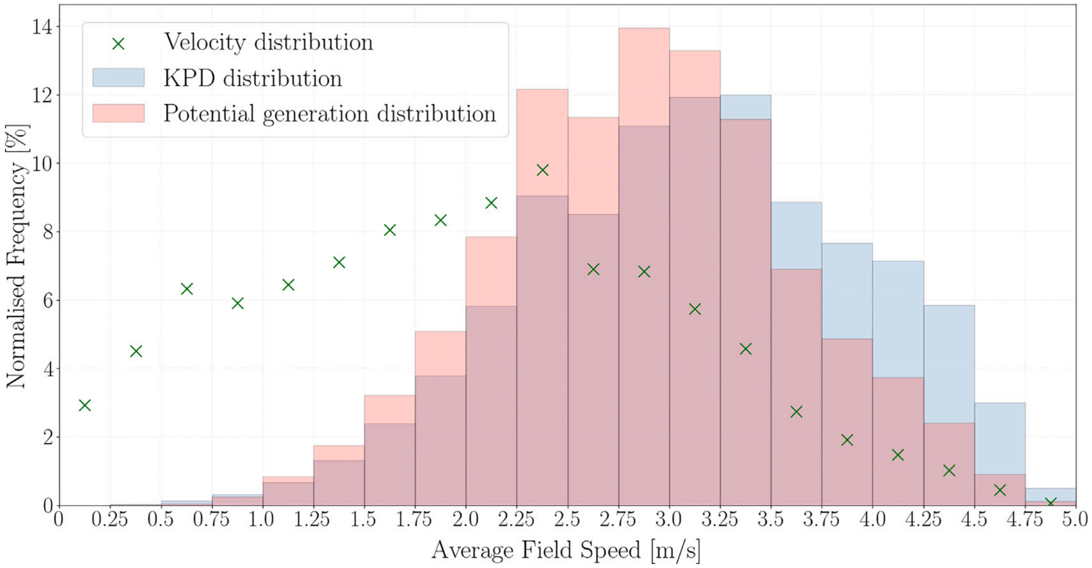

Fig. 3. Field-averaged distribution of occurrence for velocity, kinetic power density (KPD) and potential turbine power (based on AR2000 turbine) over a 28-day period.

Our objective-binning approach is then compared, targeting N flow fields that represent the ambient flow power yield for a given turbine technology as in Section 3.2 and Algorithm 1. To guide the investigation and the imposed constraints, we use a semi-realistic turbine based on the SIMEC Atlantis Energy AR2000 set-up, with a 20 m diameter, 2 MW rated power at 3.05 m/s and a cut-out speed of 5 m/s (Fig. 2). These characteristics are often neglected by several studies in Table 1 and by site feasibility investigation tools and metrics, such as Iglesias et al. [38]. Fig. 3 shows how the representation of a 28-day period varies between energy yield and kinetic power density, KPD, which is defined at a given point, m as:

$$\mathrm{KPD}(m) = \frac{1}{2}\,\rho\,|\mathbf{u}(m)|^3 \tag{13}$$

For rated turbines, KPD frequency of occurrence does not correlate with the total ambient potential power generation (as per Eq. (10)) frequency of occurrence, nor the field-averaged flow velocity frequency of occurrence. The probability distribution of energy yield shifts towards lower velocity flow fields for two reasons. Firstly, no additional power is generated above the rated speed. Secondly, turbines cease generation beyond their cut-out speed. It therefore becomes instructive to include these factors throughout the optimisation process.

Several experiments are performed on the proposed OB technique. Firstly, the number of flow fields is varied to investigate the relationship between optimised layout efficiency and the number of representative fields (N) used. Secondly, we test the influence of omitting low energy flow fields on the design. We filter flow fields where the average output of a turbine when placed across all locations is less than 10% ambient flow field capacity factor (OB-DF) (i.e. for the example turbine of our study, 0.2 MW). Finally, we assess whether the spatial variation across individual flow fields is important in the selection process. To do so, we deploy the same OB technique, using just the central point of the domain to determine the impact of the spatial variation when trying to provide a reduced temporal representation (with these cases denoted as OB-CP). These cases are summarised in Table 2.

We present yield potential roses for the central point of the deployment area alongside all points in the deployment area in Fig. 4. This is indicative of the variability present both in flow direction and energy distribution, across a portion of a potential site. A tidal rose usually consists of the joint probability of velocity directions and magnitude, the latter of which has been replaced by the potential yield (Eq. (10)) (i.e. energy conversion potential).

The turbine layout optimisation is performed using *FLORIS* as per Section 3.1.2. In order to do so the performance conditions relating to wake interaction as defined in Section 3.1.2 must be imposed, which will be sensitive to the turbine technology deployed. For the semi-realistic 2 MW turbines of Section 5.2 these are fixed between flow field selection cases, setting $B_{\max} = 0.10$ and $\Gamma_{\max} = 0.175$. The minimum capacity factor per turbine, $A_{\min}$, is calculated at each iteration of the optimisation to ensure all turbines maintain the minimum capacity factor required. This value varies between cases as a minimum capacity factor expected when only using peak flow field case would not be appropriate to use for when lower energy fields are being used. Therefore, we calculate $A_{\min}$ as 90% of the average capacity factor of the ambient flow fields for each case, $A_{\min} = 0.9 \times \frac{\min(\mathcal{O}_{\mathrm{avg}})}{P_{\mathrm{rated}}}$. For fully realistic array design, minimum longitudinal and lateral separation may be imposed depending on the specific device requirements. For the purposes of investigating the impact of the flow field selection methodology, a minimum radial separation between turbines of 2D is imposed. The flow field selection performance is evaluated by the array design efficiency, i.e. array yield, quantified in *Thetis* over the 28-day period.

4. Results

4.1. Flow field selection

Fig. 5 presents results of flow field selection through the OB methodology, when applied over a single flood and ebb tide, for demonstration purposes. Relative to an equal interval approach, flow fields are much more energetic. The percentile values indicate the cumulative ambient potential yield under the curve, highlighting the concentration of large amounts of energy over very short intervals close to the peaks.

Fig. 6 presents the field-averaged ambient energy yield capacity factor, $\frac{\mathcal{O}_{\mathrm{avg}}}{P_{\mathrm{rated}}}$, for each representative flow field selected in each case. The time-based approaches (EI, IS) lead to fields which are widely spread in terms of the objective function. Equal emphasis is placed on all fields, including those that are low in potential returns. When reducing the number of flow fields (e.g. IS6), the energetic range covered and fed to the optimisation is much reduced. In the OB approach, the range of the energies observed over the cycle is preserved until the number of flow fields is dropped below 6. The emphasis towards peak flow fields is maintained without ignoring lower energetic states which might persist for longer duration. This high concentration of energy in peak periods is demonstrated in OB36, where flow fields shift to a higher ambient capacity factor relative to IS36.

Table 2
Case descriptions for investigation of various flow field selection methodologies.

Case	Case ID	Description
Equal interval	EI-N	N flow fields at equal time intervals from a single representative flood and ebb cycle. Where $N = 3 \times 12$, 3 representative flood and ebb cycles are used.
Ignore slack	IS-N	N flow fields at equal time intervals from a single representative flood and ebb cycle, dropping any flow fields from the slack tide ($\lvert \mathbf{u}_{avg} \rvert < 1$ m/s)
Peak	P2	The flow field of maximum average speed from a representative cycle, for ebb and flood
Rated	R4	Flow fields with an average speed of just below and just above rated speed (3.05 m/s), for ebb and flood
Peak + rated	PR6	The combination of peak and rated fields (P2 + R4)
Objective binning	OB-N	N flow fields selected using Algorithm 1
Objective binning (dropping low energy fields)	OB-DF-N	N flow fields selected using Algorithm 1, but dropping any low energy fields (where average ambient yield equivalent is below 10% of the maximum potential yield)
Objective binning (central point only)	OB-CP-N	N flow fields selected using Algorithm 1, but using only the central point in the binning process, instead of field averaged values

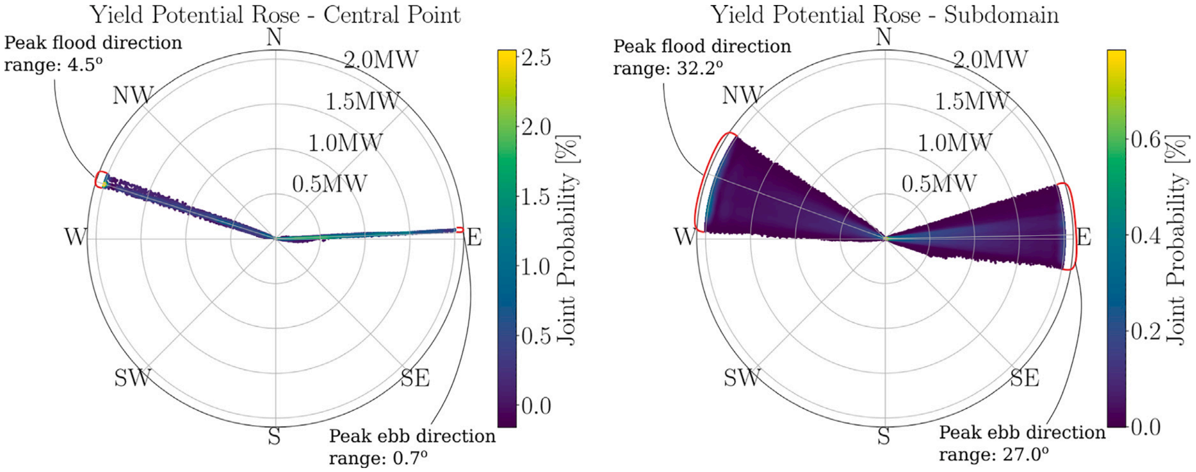

Fig. 4. Left: Potential yield rose at the central point of the deployment region. Right: Potential yield rose across the entire deployment region.

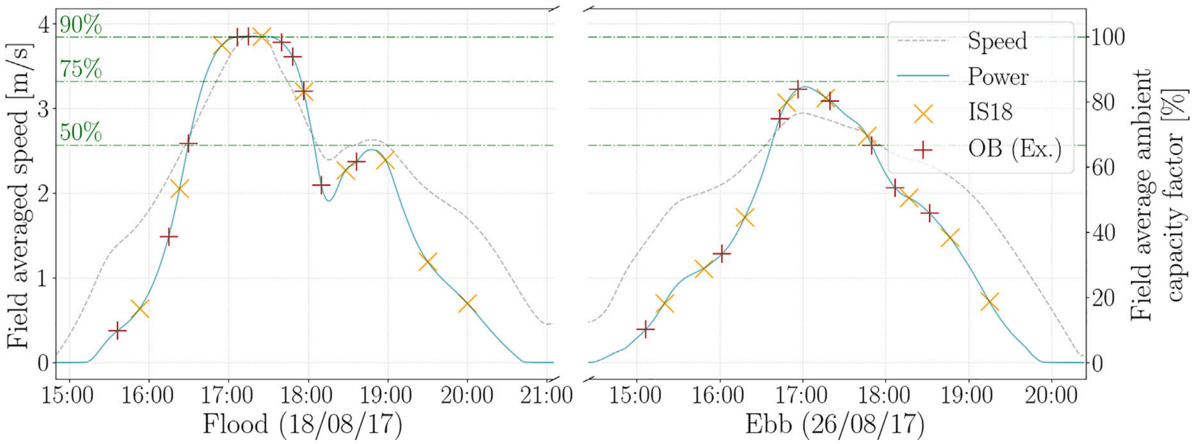

Fig. 5. Example of application of the objective binning method using two selected flow cycles. Percentage values represent the total potential yield under the curve, indicating that over 25% of the energy is held within the flood alone for these representative currents. 10% of the total ambient potential yield exists in fields with average potential capacity factor exceeding 99.7%. Note that this does not correspond to OB18, as the full 28-day period is used for the objective binning method.

The use of the flow fields in the optimisation is twofold. Firstly, the power generated and impact of each turbine added in each iteration is determined for every flow field. Secondly, flow fields are averaged to determine the next candidate turbine placement location based the highest speed and spatial constraints. Examples of time-averaged flow magnitude fields are shown in Fig. 7 for the equal interval (EI36), objective binning (OB6) and peak (P2) cases. The flow magnitude field patterns remain similar and reflective of the complex bathymetry, but the average speed of each demonstrates how bias is introduced subject to the flow field selection technique used. The turbine layouts in Fig. 7 demonstrate the consequences of the flow field selection on their distribution, whereby in the 'peak' selection, averaged flow field velocities generally exceed 3.5 m/s.Turbines in that case are subsequently placed unrealistically close together.

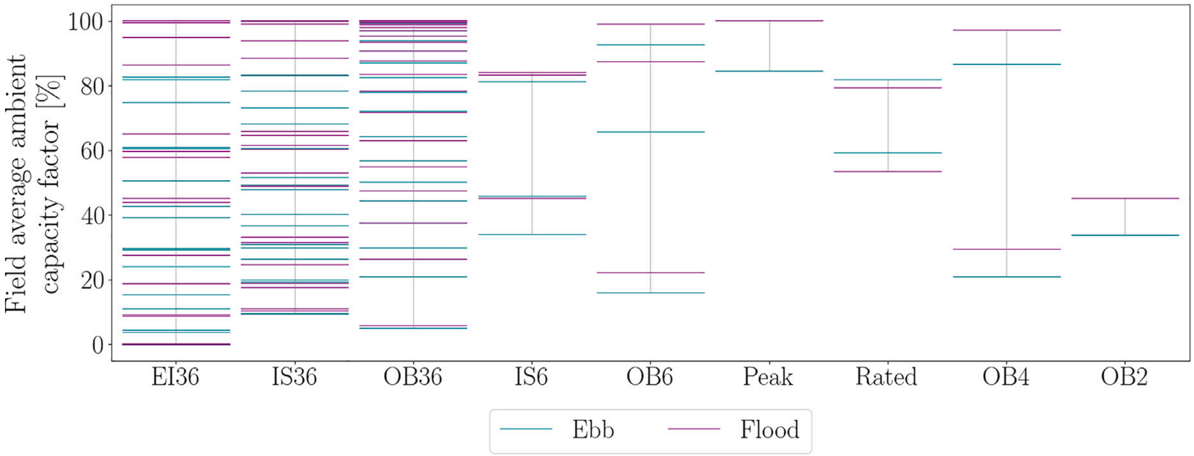

Fig. 6. Comparison of flow field ambient energy of each flow field selection method. Each line represents the flow field ambient energy of a selected flow field in terms of an equivalent capacity factor.

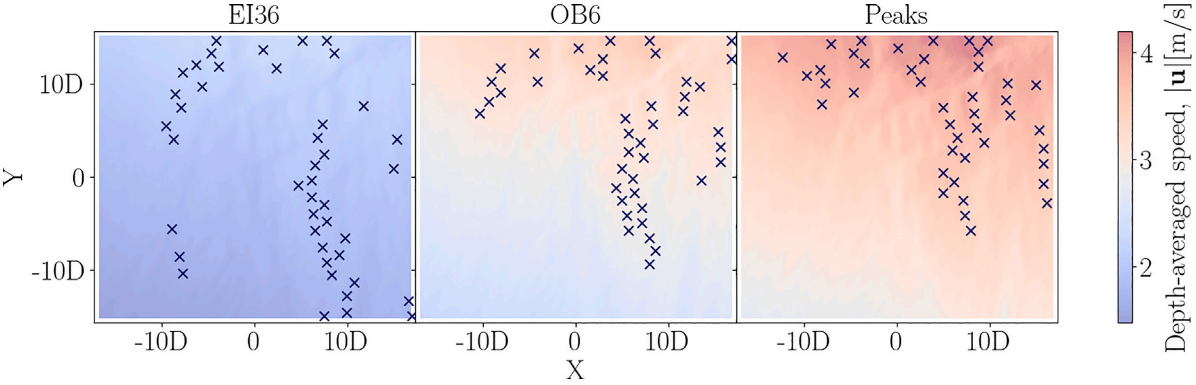

Fig. 7. Average magnitude of representative input flow fields used for array optimisation (D = 20 m). Layout of turbine coordinates for Equal Interval (EI36), Objective-Binning (OB6), and Peaks (P2) cases superimposed for completeness.

4.2. Comparison of objective binning to alternative strategies

Table 3 presents array energy yield across cases, also summarised in Fig. 8. The equal interval approach (EI36) is the least efficient method, with immediate improvement once low energy (e.g. slack period) fields are omitted. The number of flow fields used when filtering fields appears to have minimal influence on the optimised array efficiency. Using peak flow fields (P2) results in a slightly more productive optimisation process than IS cases, and is superior to using flow fields close to rated speeds (R4). The latter (R4) emphasises wake interaction avoidance in the micro-siting procedure. Combining peak flow fields with those with field-averaged speed around rated speed (PR6) leads to an overall improvement. Objective binning (OB) shows substantial improvement over alternative cases, with 6 flow fields being sufficient to generate an almost 5% improvement in array power. With the exception of case OB2, regardless of the number of flow fields selected, this method outperforms existing approaches in terms of projected array yield.

According to this analysis we make the following observations. When filtering fields below a 10% ambient field-averaged energy capacity factor prior to the OB selection procedure, array productivity improves in all cases except OB36. When using a single point (OB-CP) to guide the flow field selection instead of averaging the flow field, the array productivity decreases where a large number of flow fields are used. However, array productivity remains similar where the number of flow fields remains low. Overall, filtering low energy fields appears to be beneficial, whilst failure to exploit all of the spatial data leads to a reduction in subsequently sited array productivity. Notably, there was a failure to place all turbines when only two flow fields are used using the central point OB-CP analysis.

5. Discussion

5.1. On the impact of design constraints

Before discussion on the flow field selection methodology, we highlight a feature of the optimisation methodology that impacts the results. Design optimisation is metric-constrained to ensure that turbines do not have excessive wake interaction. In this case we use simplified formulations of such metrics to establish a minimum performance threshold ($A_{\min}$), deter excessive interaction between two devices ($B_{\max}$) and, by extension, cumulative interaction with turbines across the array ($\Gamma_{\max}$). This not only directly improves the array yield by reducing the likelihood that turbines are in lower energy wake regions, but may also assist with structural and geotechnical load requirements by proxy. These requirements could be defined (or extended) more concretely for specific devices.

The consideration of these constraints leads to several key observations. A turbine can induce a time-varying impact on a downstream turbine due to differences in thrust force, turbulence level, wake effects and broader flow variability [39]. This complicates the design optimisation, adding dimensions beyond energy yield. A simple example of the need for these constraints is when the flow speed is well above the device's rated speed. In that scenario the upstream turbine wake deficit can be insignificant in decreasing the oncoming flow speed for the downstream turbine below rated. Thus, if power generation is the

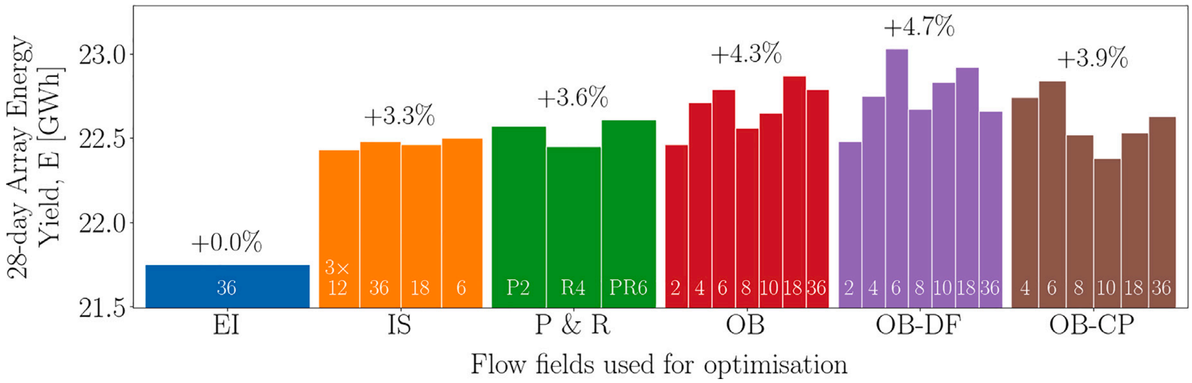

Fig. 8. Array energies for different optimisation input flow fields quantified over 28 days. OB-CP2 had insufficient turbine placements and is thus excluded.

Table 3
Results of optimisation methodology applied to each case of flow field selection. The energy yield is calculated based on array simulations of optimised layouts in *Thetis*.

Case description	No. of fields	Case ID	Yield representation index, YRI	Thetis energy yield [GWh]	
Equal interval	36	EI36	1.053	21.75	0%
Ignore slack	6	IS6	0.632	22.50	+3.45%
Ignore slack	18	IS18	0.746	22.46	+3.26%
Ignore slack	36	IS36	0.788	22.48	+3.36%
Ignore slack	3 × 12	IS3 × 12	0.680	22.43	+3.13%
Peak	2	P2	0.427	22.57	+3.77%
Rated	4	R4	0.576	22.45	+3.22%
Peak + rated	6	PR6	0.516	22.61	+3.95%
Obj. binning	2	OB2	0.996	22.46	+3.26%
Obj. binning	4	OB4	0.673	22.71	+4.41%
Obj. binning	6	OB6	0.617	22.79	+4.78%
Obj. binning	8	OB8	0.596	22.56	+3.72%
Obj. binning	10	OB10	0.574	22.65	+4.14%
Obj. binning	18	OB18	0.565	22.87	+5.15%
Obj. binning	36	OB36	0.559	22.79	+4.78%
Obj. binning (df)	2	OB-DF2	0.713	22.48	+3.36%
Obj. binning (df)	4	OB-DF4	0.598	22.75	+4.60%
Obj. binning (df)	6	OB-DF6	0.574	23.03	+5.89%
Obj. binning (df)	8	OB-DF8	0.564	22.67	+4.23%
Obj. binning (df)	10	OB-DF10	0.550	22.83	+4.97%
Obj. binning (df)	18	OB-DF18	0.548	22.92	+5.38%
Obj. binning (df)	36	OB-DF36	0.546	22.66	+4.18%
Obj. binning (cp)	2	OB-CP2	0.995	*	*
Obj. binning (cp)	4	OB-CP4	0.625	22.74	+4.55%
Obj. binning (cp)	6	OB-CP6	0.542	22.84	+5.01%
Obj. binning (cp)	8	OB-CP8	0.530	22.51	+3.49%
Obj. binning (cp)	10	OB-CP10	0.525	22.38	+2.90%
Obj. binning (cp)	18	OB-CP18	0.511	22.53	+3.59%
Obj. binning (cp)	36	OB-CP36	0.510	22.63	+4.05%

*Failure to place all turbines.

sole driver, then for a small number of flow fields, a high energy field will dominate the optimisation process. This was the case in [26], where metrics were calculated once per iteration based on the average power across all flow fields. There, flow fields were empirically selected around rated speed. This analysis demonstrates how such practices may lead design to a relatively narrow energetic range (see Fig. 6, case Rated (R4)).

Conversely, in [25], constraints were prescribed for each flow field. This instead allows a subset of extreme low-energy flow fields to dominate the acceptance/rejection of candidate turbine coordinates. A balance must be satisfied across these extremes, and care should be directed to the formulation of the metrics that assess compliance to the optimisation constraints. To do so, the metric average was tested herein. Using the constraint metric average still risks an emphasis on one of the dominant flow directions (i.e. if a particular metric is at 4% in one direction, and 12% in the other direction, an average of 8% would satisfy a 10% requirement). However, sensitivity tests found using the average of the field metrics superior for power yield to requiring all, or a subset of the flow fields to be compliant (or a combination of both). Whilst this metric-averaged based approach step prevents any particular flow field overly governing design, the optimisation remains more sensitive the fewer the flow fields used, as each field has a larger impact on the average metric value.

These complications arise as constraints beyond energy yield are factored in the optimisation requiring engineering judgement to inform the metrics that converge to the final design.

5.2. *On the impact of flow field selection on optimisation*

Several approaches (Table 2) were tested to guide the instantaneous flow field selection and inform the optimisation process. We see a close sensitivity of these inputs and the final layout. Applying a uniform discretisation to flow field selection over a spring-neap tidal cycle (EI) performs poorly due to the inclusion of several low-energetic fields

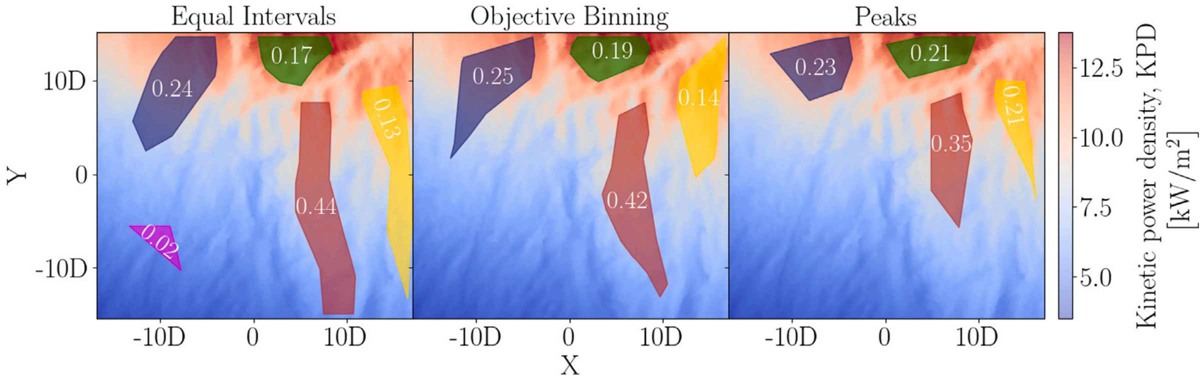

Fig. 9. Array regions superimposed onto the 28-day average potential energy field (based on AR2000, D = 20 m). Numerical values represent the proportion of turbines within each region.

that penalise the acceptance of turbines in close proximity. This leads to excessive spacing and thus an overly conservative, wake avoidance focussed layout design. Filtering slack tide and low capacity fields as in [25], leads to an array that is 3% more productive on average. By switching the optimisation performance conditions to those of Jordan et al. [26], this discrepancy could be avoided as discussed in Section 5.1, though at reduced optimisation efficiency. With the capability of applying performance conditions as in-place here, extensions could adapt optimisation constraints (that in this case balance turbine–turbine interaction and turbine–array interaction) subject to the average flow speed of each field. An alternative option would be to weigh the importance of constraints based on the frequency of occurrence of each flow field, akin to the proposed OB method.

One benefit of the OB method is that we can minimise the number of flow fields used where the optimisation space is already very large. Funke et al. [12] deployed an adjoint-based optimisation method in a steady state simulation, which required days of run time to complete on a supercomputer. When applying such approaches over transient periods, the shorter the model run time, the lesser the computational cost. A route to identify representative subsets of the flow could be extremely beneficial in reducing memory and time for such approaches. Metric-based approaches require hyper-parameterisation, particularly when optimisations become multi-objective. Fundamentally, it is desirable to minimise the flow field number, N, used in optimisation. Even surrogate models (i.e. in this case, FLORIS) become time-consuming for large-scale, finely resolved domains with multiple objectives over non-linear parameter spaces. This is particularly important when the array deployment area increase is proportional to the memory requirements dedicated to perform optimisation.

Fig. 9 presents the primary regions where turbines are deployed subject to different cases. On EI/IS cases for flow field selection, emphasis is primarily placed on wake avoidance. Equal emphasis is placed on all fields, adding more frequent lower energy fields that bias the optimisation process. Conversely, by relying solely on peak flow fields, turbines are densely packed into high-energy regions, promoting more wake interaction. The OB technique emphasises representation of the flow based on the energy and subsequently provides the means to achieve a critical balance between array density in high energy regions and wake avoidance.

5.3. On the sensitivity of the proposed methodology

We explored the significance of including low energy flow fields, typically associated with slack periods. In removing these fields prior to OB flow field selection, we see an increased array productivity, generally. OB essentially weights each flow field equally so that the cycle is represented in terms of energy, as fairly as possible. In omitting high-frequency lower energy fields, it becomes logical that we may lose balance in establishing an optimal layout. The primary difference when filtering low energy fields regards the final representative fields selected as inputs in the optimisation. The most energetic flow field bins are the smallest, as high levels of energy are concentrated in short periods. Therefore the first-selected fields are similar regardless of whether low energy fields are excluded or not. The representative fields selected at lower energy bins subsequently see a larger variation in velocity. Where flow data stemming from the full cycle is used (e.g. EI), a flow field with average direction varying notably from the principal current direction may be used. For small numbers of flow fields, this could influence whether a turbine is accepted or rejected. Considering additional similarity indices and further refining constraints could reject selection of such fields in the OB method. This is beyond the scope of the work presented here and also appears to be dealt with by removal of these fields (OB-DF).

With increasing flow field number, N, optimisation sensitivity reduces. However, the number of energy bins increases and this leads to more selected flow fields that are of higher energy. Here, interaction metrics should be reviewed or modified per flow field, since higher energetic flow fields are easier to satisfy power-related constraints even when turbines interact. In this study, we fixed interaction related metrics, $B_{\max}$ and $\Gamma_{\max}$, for ease of explanation. A potential issue emerges by increasing emphasis on higher energy fields leads to, say, a 3% benefit for those fields, at the cost of a 5% loss in productivity over low energetic states. This is demonstrated in Fig. 10, where filtering low energy fields leads to improved yield during peak flood flow but substantial reductions in the peak-slack transition.

Using a velocity time-series at a single or limited points to determine optimisation flow fields is common in wind farm layout optimisation (e.g. Samorani [40],Cazzaro and Pisinger [41]). A similar “tidal rose” approach is used in [21,27]. While acceptable for wind farms where ambient velocity does not fluctuate substantially, significantly greater variability in space is encountered in a tidal domain. This is demonstrated herein in Fig. 4 for a relatively compact site. The influence of losing this spatial variability in the flow field selection process for tidal stream energy application subsequently impacts the temporal variability observed. Excluding cases where optimisation is more sensitive to the low number of flow fields, we see a subtle but noticeable drop in array productivity as a result. This also highlights the challenge of capturing the spatial variation accurately in hydrodynamic models, due to the limited observation points available across tidal sites. Further work would entail the examination of this effect across different sites and quantifying the significance of the point used, when the spatial variation is not considered.

5.4. On the limitations of the study

A few intricacies were not explored in this study, such as the impact of post-cut-out speeds. Over spring tide peaks at certain parts of the

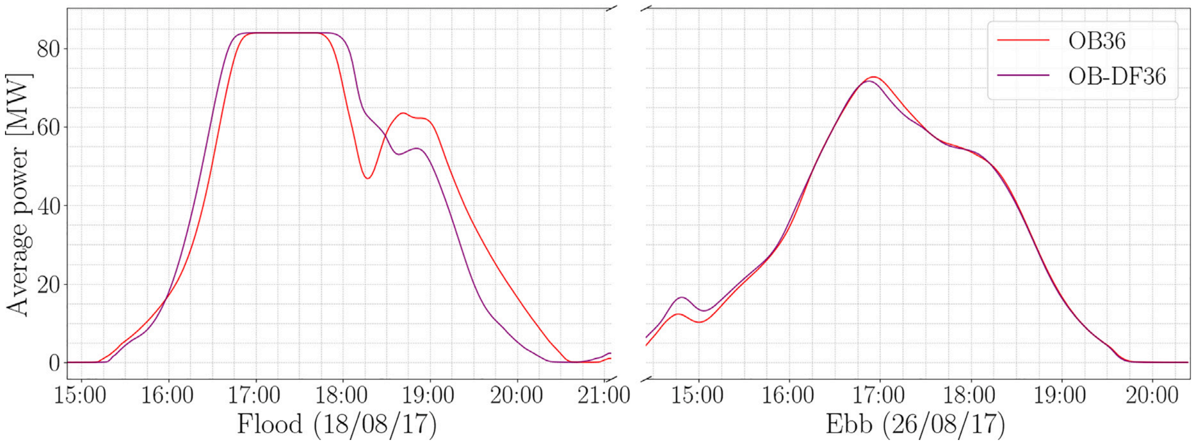

Fig. 10. Array power comparisons over representative flood and ebb cycles for cases OB36 and OB-DF36.

Inner Sound, occasions arise where flow speed exceeds 5 m/s. Where these flow speeds are recorded, the objective function will take a value of zero, subsequently leading to $\frac{\mathcal{O}_{avg}}{P_{\text{rated}}} < 1$ despite a field exhibiting peak flow. Therefore, it could enter a bin with lower objective value, in spite of being one of the most energetic fields present over the time investigated. This is a result of the objective function being tailored to the device capabilities. This can therefore interfere with the optimisation balance desired. Another issue requiring further exploration is when the deployment area considered becomes larger, such that the lag between peak velocities across the site becomes notable. This can lead to bias towards certain regions and therefore for sites on the potential scale of hundreds of turbines, adjustments would need to be made to this method to avoid this bias.

Further exploration is also required for the special case of using only two flow fields (e.g. OB-DF2) where the OB technique is inefficient. This is because no binning is actually performed when limited to a single flow field for each ebb and flood tide. In the current implementation, the field corresponding to the average value for each bin will be used, which will statistically be of a relatively low energy. Therefore, one modification to potentially improve the OB technique without a specific methodology for this case, is to change the method of flow field selection for each bin. This entails using the field that corresponds to the 50% point in cumulative energy, rather than the 50% value of power. This special case is of particular interest where instead of instantaneous flow fields whole cycles must be identified to capture the transient dynamic features. Including transient runs such as through adjoint-based optimisation will have higher memory requirements, and thus further work should explore a strategy towards a representative cycle selection for optimisation. This is another limitation of the study, as only the custom greedy algorithm has been deployed, which has its own limitations as discussed in [25]. Instead, we present the implications of the use of the flow field methodology for other optimisation strategies in Appendix C.

6. Conclusions

We present a statistical objective-driven approach to provide a reduced representation of tidal flow. This is applied in the context of tidal array optimisation, where the objective driven approach selects instantaneous flow fields or cycles based on realisable energy of specific device characteristics. Flow field selection has previously been performed empirically, which we show here to have tangible implications for array shape and size. Also, the objective-driven method results in an array optimisation procedure that is 4%–5% more productive than simply using unweighted transient approaches (and up to 2% improvement against using peak flow fields), for a metric-based optimisation of the Inner Sound of the Pentland Firth. The statistical approach ensures that the inputs presented to the optimisation procedure offer a fair representation in terms of the desired objective (e.g. energy, yield), instead of the frequency of occurrence of simpler parameters used for model calibration (e.g. velocity). This approach subsequently reduces potential losses in array capacity factor in the optimisation, in addition to demonstrating that a reduced number of flow fields can be used in this process without loss in the final optimisation objective function. We find that the spatial variability of the flow is influential in flow field selection, as use of a single point in selecting representative flow fields leads to less productive arrays. This is significant as array sites are often insufficiently resolved and their potential is assessed in models based on a single time series.

Whilst this work has been conducted for tidal array resource, it serves as a useful approach for reduced modelling for any non-linear objective function where the frequency of primary parameters (i.e. velocity, depth) are not suitable for selecting flow fields for analysis or control/optimisation.

CRediT authorship contribution statement

Connor Jordan: Writing – review & editing, Writing – original draft, Visualization, Validation, Software, Methodology, Investigation, Formal analysis, Conceptualization, Funding acquisition. **Joseba Agirre:** Writing – review & editing, Visualization, Methodology, Investigation, Formal analysis. **Athanasios Angeloudis:** Writing – review & editing, Supervision, Software, Resources, Project administration, Methodology, Funding acquisition.

Declaration of competing interest

The authors declare that they have no known competing financial interests or personal relationships that could have appeared to influence the work reported in this paper.

Acknowledgements

C. Jordan acknowledges the support of EPSRC, UK through a Ph.D. studentship and the IAA PV182 ATARI project under grant agreement EP/X525698/1. J. Agirre acknowledges funding from the School of Engineering, University of Edinburgh, UK. A. Angeloudis acknowledges the support of the EC H2020 ILIAD DTO project under grant agreement 101037643. The authors would like to thank all researchers who contributed to checking the contents of Table 1 are correct. Finally, we would also like to thank the anonymous reviewers for their diligent comments that have substantially improved the clarity of the manuscript during the review process.

Appendix A. Array design algorithm

Algorithm 2 describes the process for array design within *FLORIS*. At each iteration, the location of highest energy is determined and a turbine is added to the array. If each turbine within the array satisfies the constraints defined, then the turbine is accepted. Each accepted or rejected turbine then masks the selection process for the next iteration. This algorithm completes once the number of desired turbines within the array is finished, or when the solution region has been fully explored.

Algorithm 2 Sequential addition of turbines to domain using greedy optimisation.

CONDITIONS: Each turbine must meet a minimum A-% average turbine capacity factor, have maximum reduction of power to any other turbine of B-% and maximum reduction of power to the sum of individual turbines (that face power output reductions) of Γ-%.

CONSTRAINTS (Δ, E): Minimum distance constraints for turbine placement, specified in turbine diameters away from considered coordinate.

```
while iteration no. < maximum no. of iterations do
    while no. of turbines < maximum no. of turbines do
        Calculate and add turbine wakes to each flow field of selected tidal cycles.
        Calculate a moving average flow magnitude field (a moving average deters turbine placements on wake edges).
        Identify coordinate of highest average velocity magnitude as a candidate turbine location.
        Add turbine at candidate site and impose wake on each flow field of selected tidal cycles.
        Calculate the average power (using each individual field) for all turbines including the new turbine.
        if CONDITIONS are met then
            Add candidate site to list of accepted coordinates.
            Impose a restriction for turbine placement within a limiting distance $\Delta$ around new coordinate.
        else
            Add candidate site to list of blocked coordinates.
            Impose a restriction for turbine placement within a limiting distance of $E$ around blocked coordinate.
        end if
    end while
end while
```

Appendix B. Analytical wake modelling using *FLORIS*

FLORIS utilises a number of analytical models to predict the mean wake velocities and power output of turbine arrays [42]. In the present study, we make use of FLORIS's Gaussian model originally introduced by Bastankhah and Porté-Agel [34] which computes the normalised velocity deficit via the expression

$$\frac{\Delta U}{U_\infty} = \left(1 - \sqrt{1 - \frac{C_T}{8\left(k^* x/d_0 + \epsilon\right)^2}}\right) \times e^{\left(-\frac{1}{2\left(k^* x/d_0+\epsilon\right)^2}\left\{\left(\frac{z-z_h}{d_0}\right)^2+\left(\frac{y}{d_0}\right)^2\right\}\right)}, \tag{B.1}$$

where U_∞ is the approaching streamwise velocity, z is the wall-normal coordinate with z_h the turbine hub height, k^* is the growth rate of the wake $(\partial\sigma/\partial x)$, d_0 is the diameter of the wind turbine and ϵ is the normalised Gaussian velocity deficit at the rotor plane. For our calculations the local wake growth rate k^* is estimated using the local streamwise turbulence intensity, $\mathcal{I}$ [43]. Turbine power output on the other hand, is calculated using a power thrust–velocity relationship specified for each individual turbine. This requires a combination model to account for the contributing wake velocity deficit from upstream and other neighbouring turbines. Here, we have selected to use the free-stream linear superposition (FLS) method to account for the cumulative wake effects within the tidal array. The velocity deficit, $\overline{\Delta\mathbf{u}}(x, y)$, at a downstream location (x, y) is calculated as,

$$\overline{\Delta\mathbf{u}}(x, y) = \sum_{i=1}^{N}\left(\overline{\Delta\mathbf{u}}_i|_{(x,y)}\right), \tag{B.2}$$

where $\overline{\Delta\mathbf{u}}_i|_{(x,y)}$ is the contribution the wake of each turbine i at the downstream location (x, y) [44].

Table B.4
Calibrated wake parameters for Gaussian model, with support structure included in *Thetis*.

k_a	0.002173
k_b	0.02272
α	0.5751
β	0.2974

Wake-specific parameters for the AR2000 turbine were calibrated in [26] to replicate the velocity deficits exhibited when modelled in *Thetis*. These include k_a and k_b, parameters that relate to turbulence intensity and wake width. These combine and determine the value of the wake growth rate, k^*, which eventually enters the Gaussian velocity deficit Eq. (B.1) calculated as,

$$k^* = k_a \cdot \mathcal{I} + k_b. \tag{B.3}$$

The second set of parameters α and β are used for the quantity, x_0, which defines the onset of the far wake,

$$x_0 = D\frac{1 + \sqrt{1 - C_t}}{\sqrt{2}\left(4\alpha \cdot \mathcal{I} + 2\beta\left(1 - \sqrt{1 - C_t}\right)\right)}. \tag{B.4}$$

Calibration was performed using differential evolution (as implemented within SciPy's optimisation library [45]) as described in [25]. The final parameters are presented in Table B.4.

Appendix C. On alternative optimisation methodologies and implications for the micro-siting process

We can make several inferences on the potential impact of this flow field methodology on other studies from the discussion presented in Section 5.2. In [24], turbine positions were restricted based on a structured grid, so we might expect that turbines are too closely spaced as a result of using only the peak flood and ebb fields. Similarly, in [12], only a singular flood steady state simulation was used with the primary objective being the demonstration of the adjoint methodology. Whilst the application was unrealistic, we can still hypothesise that if more appropriate flow fields were used by the OB method or if a flood/ebb tidal cycle was used with energy as the objective, we would see larger spacing between rows of turbines whilst still exploiting array scale blockage. In [22,23], optimal array structure spacings are found by using mathematical functions to estimate the predicted yield of a turbine given a set number of prescribed model runs. In this setting, we can take advantage of the OB method to use minimal computationally expensive steady-state 3D model runs and subsequently achieve results that are reflective of the temporal complexities present in marine problems. This can be further extended to large eddy simulation studies such as Ouro et al. [46], where the selection of time period is critical due to the computational cost.

To deal with the temporal variation in tidal flows [21] or [27] made use of a "tidal rose". However, in these approaches the flow field velocity is kept uniform, thus only targeting wake interaction minimisation whilst failing to deal with the inherent spatial variation in the ambient condition. Nonetheless, the methodology of Lo Brutto et al. [21] still takes an initial step towards a better representation of the flow when using a combination of the instantaneous power as an objective by introducing a weighting based on the frequency of occurrence. With the OB method we can substantially reduce the number of fields used, and rather than using velocity, we use an objective function related to the optimisation objective, which is a better representation of the flow for layout optimisation purposes.

Whilst this methodology has been applied in the context of instantaneous flow field selection, similar results are expected when applied to simultaneous placement and full-cycle approaches to optimisation. For example, Zhang et al. [17] performed optimisation for neap, intermediate and spring tides and found that the optimal turbine density changes depending on the tides used. A continuous representation of the array was used and the number of turbines was not set, thus the results are not directly comparable to the work presented here, but nevertheless support the hypothesis that there must be an optimal period for micro-siting. During neap tides, where velocity magnitudes are low, the optimisation compensated by increasing the density to fill the entire deployment area. As velocity magnitude increases, the turbine density becomes more consistent. In this case, lack of rated and cut-out speeds may impact this result, hence the benefit of using the OB method to select optimal cycles for realistic turbine specifications. However, for studies such as Phoenix and Nash [29], where a spring cycle is used with discrete, realistic turbine representation, we might anticipate too much emphasis on high-density packing of turbines. In addition, not only is there variation over a lunar month, Thiébot et al. [2] estimated that over an 18.6 year cycle, there is a variation of up to ±10% in KPD per year. This may also have implications for harnessing local and array scale blockage effects that lead to higher flow speeds and potentially support denser array configurations, as demonstrated in [16].

Array layout is not contingent only on energy. In [18], environmental impacts were studied through the form of minimising the velocity deficit incurred by the array, using a steady state peak flood field to minimise computational cost whilst demonstrating the methodology. However, the lack of temporal variability presents a flaw not only in the optimisation, as the array layout will change substantially with the introduction of the ebb tide, but also a flaw in obtaining the Pareto front. The Pareto front is used in multi-objective optimisation to describe the set of solutions that satisfy all of the objectives efficiently. At the ‘middle’ of the Pareto front, the solution may solve all objectives with equal emphasis on each. Without the temporal variability included, the array will tend towards over-packing into energetic regions, and thus the Pareto front will shift further toward minimising overall array deficit, which is achieved by increasing turbine-array interaction. This is complicated in [18] by allowing turbines to be placed one on top of the other and in [19] by continuous representation of the array. Should temporal variability be included, a more accurate and balanced Pareto front that satisfies both objectives should be obtained. This also applies for any studies where LCOE is formulated within the optimisation objective function with a weighting factor between profitability and power such as Goss et al. [15] or Culley et al. [13]. Examining Goss et al. [15], a highly simplified headland channel model was used to demonstrate how array layouts change in response to varying economic parameters. Again, as the objective is primarily to demonstrate a methodology, we can only hypothesise how results would vary for application with realistic spatial and temporal representation. However, the use of only an M2 like signal means that each cycle is identical and we sacrifice array performance over the full lifecycle of a project by optimisation that does not consider the full spatio-temporal complexity of the problem. We can anticipate that correct choice of cycle for optimisation would be critical for an accurate emulator and a better balanced Pareto front.

Regardless of optimisation methodology and constraints, array productivity is contingent on the three key factors outlined in Section 3. These can all be linked to the spatio-temporal variation of the problem, and thus balanced array design will not be achieved without using a representative cycle and corresponding optimal metrics, where used.

References

[1] B. Polagye, J. Thomson, Tidal energy resource characterization: methodology and field study in Admiralty Inlet, Puget Sound, WA (USA), Proc. Inst. Mech. Eng. A 227 (3) (2013) 352–367, http://dx.doi.org/10.1177/0957650912470081.

[2] J. Thiébot, S. Guillou, E. Droniou, Influence of the 18.6-year lunar nodal cycle on the tidal resource of the Alderney Race, France, Appl. Ocean Res. 97 (2020) 102107, http://dx.doi.org/10.1016/j.apor.2020.102107, URL https://www.sciencedirect.com/science/article/pii/S0141118719310132.

[3] J. Thiébot, N. Guillou, D. Coles, S. Guillou, On nodal modulations of tidal-stream energy resource in north-western Europe, Appl. Ocean Res. 121 (2022) 103091, http://dx.doi.org/10.1016/j.apor.2022.103091, URL https://www.sciencedirect.com/science/article/pii/S0141118722000451.

[4] T. Monahan, T. Tang, T.A. Adcock, A hybrid model for online short-term tidal energy forecasting, Appl. Ocean Res. 137 (2023) 103596, http://dx.doi.org/10.1016/j.apor.2023.103596, URL https://www.sciencedirect.com/science/article/pii/S0141118723001372.

[5] S.C. Warder, S.C. Kramer, M.D. Piggott, Non-deterministic effects in modelling the tidal currents in a high-energy coastal site, 2021, http://dx.doi.org/10.31223/X55G7F, Preprint on Earth ArXiv.

[6] K. Pappas, L. Mackie, I. Zilakos, A.H. van der Weijde, A. Angeloudis, Sensitivity of tidal range assessments to harmonic constituents and analysis timeframe, Renew. Energy 205 (2023) 125–141, http://dx.doi.org/10.1016/j.renene.2023.01.062, URL https://www.sciencedirect.com/science/article/pii/S096014812300071X.

[7] S.P. Neill, M.R. Hashemi, M.J. Lewis, The role of tidal asymmetry in characterizing the tidal energy resource of Orkney, Renew. Energy 68 (2014) 337–350, http://dx.doi.org/10.1016/j.renene.2014.01.052, URL https://www.sciencedirect.com/science/article/pii/S0960148114000998.

[8] M. Thiébaut, A. Sentchev, Asymmetry of tidal currents off the W.Brittany coast and assessment of tidal energy resource around the Ushant Island, Renew. Energy 105 (2017) 735–747, http://dx.doi.org/10.1016/j.renene.2016.12.082, URL https://www.sciencedirect.com/science/article/pii/S0960148116311417.

[9] P. Evans, A. Mason-Jones, C. Wilson, C. Wooldridge, T. O’Doherty, D. O’Doherty, Constraints on extractable power from energetic tidal straits, Renew. Energy 81 (2015) 707–722, http://dx.doi.org/10.1016/j.renene.2015.03.085, URL https://www.sciencedirect.com/science/article/pii/S0960148115002761.

[10] F. Orgeret, A. Thiebault, K.M. Kovacs, C. Lydersen, M.A. Hindell, S.A. Thompson, W.J. Sydeman, P.A. Pistorius, Climate change impacts on seabirds and marine mammals: The importance of study duration, thermal tolerance and generation time, Ecol. Lett. 25 (1) (2022) 218–239, http://dx.doi.org/10.1111/ele.13920, arXiv:https://onlinelibrary.wiley.com/doi/pdf/10.1111/ele.13920.

[11] K. Gunn, C. Stock-Williams, On validating numerical hydrodynamic models of complex tidal flow, Int. J. Mar. Energy 3–4 (2013) e82–e97, http://dx.doi.org/10.1016/j.ijome.2013.11.013, URL https://www.sciencedirect.com/science/article/pii/S2214166913000398, Special Issue – Selected Papers - EWTEC2013.

[12] S. Funke, P. Farrell, M. Piggott, Tidal turbine array optimisation using the adjoint approach, Renew. Energy 63 (2014) 658–673, http://dx.doi.org/10.1016/j.renene.2013.09.031.

[13] D. Culley, S. Funke, S. Kramer, M. Piggott, Integration of cost modelling within the micro-siting design optimisation of tidal turbine arrays, Renew. Energy 85 (2016) 215–227, http://dx.doi.org/10.1016/j.renene.2015.06.013.

[14] M.D. Piggott, S.C. Kramer, S. Funke, D. Culley, A. Angeloudis, Optimization of marine renewable energy systems, in: Comprehensive Renewable Energy, Elsevier BV, 2022, pp. 176–220.

[15] Z.L. Goss, D.S. Coles, S.C. Kramer, M.D. Piggott, Efficient economic optimisation of large-scale tidal stream arrays, Appl. Energy 295 (2021) 116975, http://dx.doi.org/10.1016/j.apenergy.2021.116975, URL https://www.sciencedirect.com/science/article/pii/S0306261921004475.

[16] S. Funke, S. Kramer, M. Piggott, Design optimisation and resource assessment for tidal-stream renewable energy farms using a new continuous turbine approach, Renew. Energy 99 (2016) 1046–1061, http://dx.doi.org/10.1016/j.renene.2016.07.039, URL https://www.sciencedirect.com/science/article/pii/S0960148116306358.

[17] J. Zhang, C. Zhang, A. Angeloudis, S.C. Kramer, R. He, M.D. Piggott, Interactions between tidal stream turbine arrays and their hydrodynamic impact around Zhoushan Island, China, Ocean Eng. 246 (2022) 110431, http://dx.doi.org/10.1016/j.oceaneng.2021.110431, URL https://www.sciencedirect.com/science/article/pii/S0029801821017170.

[18] R. du Feu, S. Funke, S. Kramer, D. Culley, J. Hill, B. Halpern, M. Piggott, The trade-off between tidal-turbine array yield and impact on flow: A multi-objective optimisation problem, Renew. Energy 114 (2017) 1247–1257, http://dx.doi.org/10.1016/j.renene.2017.07.081, URL https://www.sciencedirect.com/science/article/pii/S0960148117307097.

[19] R. du Feu, S. Funke, S. Kramer, J. Hill, M. Piggott, The trade-off between tidal-turbine array yield and environmental impact: A habitat suitability modelling approach, Renew. Energy 143 (2019) 390–403, http://dx.doi.org/10.1016/j.renene.2019.04.141, URL https://www.sciencedirect.com/science/article/pii/S0960148119306251.

[20] C. Zhang, S.C. Kramer, A. Angeloudis, J. Zhang, X. Lin, M.D. Piggott, Improving tidal turbine array performance through the optimisation of layout and yaw angles, Int. Mar. Energy J. 5 (3) (2022) 273–280, http://dx.doi.org/10.36688/imej.5.273-280, URL https://marineenergyjournal.org/imej/article/view/119.

[21] O.A. Lo Brutto, J. Thiébot, S.S. Guillou, H. Gualous, A semi-analytic method to optimize tidal farm layouts – Application to the Alderney Race (Raz Blanchard), France, Appl. Energy 183 (2016) 1168–1180, http://dx.doi.org/10.1016/j.apenergy.2016.09.059, URL https://www.sciencedirect.com/science/article/pii/S0306261916313617.

[22] E. González-Gorbeña, R.Y. Qassim, P.C. Rosman, Optimisation of hydrokinetic turbine array layouts via surrogate modelling, Renew. Energy 93 (2016) 45–57, http://dx.doi.org/10.1016/j.renene.2016.02.045, URL https://www.sciencedirect.com/science/article/pii/S096014811630146X.

[23] E. González-Gorbeña, R.Y. Qassim, P.C. Rosman, Multi-dimensional optimisation of Tidal Energy Converters array layouts considering geometric, economic and environmental constraints, Renew. Energy 116 (2018) 647–658, http://dx.doi.org/10.1016/j.renene.2017.10.009.

[24] G.-w. Wu, H. Wu, X.-y. Wang, Q.-w. Zhou, X.-m. Liu, Tidal turbine array optimization based on the discrete particle swarm algorithm, China Ocean Eng. 32 (2018) 358–364, http://dx.doi.org/10.1007/s13344-018-0037-6.

[25] C. Jordan, D. Dundovic, A.K. Fragkou, G. Deskos, D.S. Coles, M.D. Piggott, A. Angeloudis, Combining shallow-water and analytical wake models for tidal array micro-siting, J. Ocean Eng. Mar. Energy 8 (2) (2022) http://dx.doi.org/10.1007/s40722-022-00225-2.

[26] C. Jordan, D. Coles, F. Johnson, A. Angeloudis, On tidal array layout sensitivity to regional and device model representation, in: Proceedings of the European Wave and Tidal Energy Conference, Vol. 15, 2023, http://dx.doi.org/10.36688/ewtec-2023-302, URL https://submissions.ewtec.org/proc-ewtec/article/view/302.

[27] M.A. Mubarok, N.R. Arini, D. Satrio, Optimization of horizontal axis tidal turbines farming configuration using particle swarm optimization (PSO) algorithm, in: 2023 International Electronics Symposium, IES, 2023, pp. 19–25, http://dx.doi.org/10.1109/IES59143.2023.10242450.

[28] T. Divett, R. Vennell, C. Stevens, Channel-scale optimisation and tuning of large tidal turbine arrays using LES with adaptive mesh, Renew. Energy 86 (2016) 1394–1405, http://dx.doi.org/10.1016/j.renene.2015.09.048, URL https://www.sciencedirect.com/science/article/pii/S096014811530327X.

[29] A. Phoenix, S. Nash, Optimisation of tidal turbine array layouts whilst limiting their hydro-environmental impact, J. Ocean Eng. Mar. Energy 5 (3) (2019) 251–266, http://dx.doi.org/10.1007/s40722-019-00145-8.

[30] T. Kärnä, S.C. Kramer, L. Mitchell, D.A. Ham, M.D. Piggott, A.M. Baptista, Thetis coastal ocean model: discontinuous Galerkin discretization for the three-dimensional hydrostatic equations, Geosci. Model Dev. Discuss. 2018 (2018) 1–36, http://dx.doi.org/10.5194/gmd-2017-292, URL https://www.geosci-model-dev-discuss.net/gmd-2017-292/.

[31] F. Rathgeber, D.A. Ham, L. Mitchell, M. Lange, F. Luporini, A.T.T. Mcrae, G.-T. Bercea, G.R. Markall, P.H.J. Kelly, Firedrake: Automating the finite element method by composing abstractions, ACM Trans. Math. Software 43 (3) (2016) 24:1–24:27, http://dx.doi.org/10.1145/2998441, URL http://doi.acm.org/10.1145/2998441.

[32] L. Mackie, P.S. Evans, M.J. Harrold, T. O‘Doherty, M.D. Piggott, A. Angeloudis, Modelling an energetic tidal strait: investigating implications of common numerical configuration choices, Appl. Ocean Res. 108 (January) (2021) 102494, http://dx.doi.org/10.1016/j.apor.2020.102494.

[33] S.C. Kramer, M.D. Piggott, A correction to the enhanced bottom drag parameterisation of tidal turbines, Renew. Energy 92 (2016) 385–396.

[34] M. Bastankhah, F. Porté-Agel, A new analytical model for wind-turbine wakes, Renew. Energy 70 (2014) 116–123, http://dx.doi.org/10.1016/j.renene.2014.01.002.

[35] Department for Energy Security and Net Zero, Contracts for Difference (CfD) Allocation Round 5: results, 2023, https://www.gov.uk/government/publications/contracts-for-difference-cfd-allocation-round-5-results, (Accessed: 03/10/2023).

[36] Edina Digimap Service, Hydrospatial one, gridded bathymetry, 2020, http://digimap.edina.ac.uk/marine/, SeaZone Solutions Ltd, Online; accessed 2020.

[37] G.D. Egbert, S.Y. Erofeeva, Efficient inverse modeling of barotropic ocean tides, J. Atmos. Ocean. Technol. 19 (2) (2002) 183–204, http://dx.doi.org/10.1175/1520-0426(2002)019<0183:EIMOBO>2.0.CO;2.

[38] G. Iglesias, M. Sánchez, R. Carballo, H. Fernández, The TSE index – A new tool for selecting tidal stream sites in depth-limited regions, Renew. Energy 48 (2012) 350–357, http://dx.doi.org/10.1016/j.renene.2012.05.012, URL https://www.sciencedirect.com/science/article/pii/S0960148112003333.

[39] S. Lee, M. Churchfield, P. Moriarty, J. Jonkman, J. Michalakes, Atmospheric and wake turbulence impacts on wind turbine fatigue loadings, in: Proceedings of the 50th AIAA Aerospace Sciences Meeting Including the New Horizons Forum and Aerospace Exposition, 2012, pp. 1–13, http://dx.doi.org/10.2514/6.2012-540, arXiv:https://arc.aiaa.org/doi/pdf/10.2514/6.2012-540, URL https://arc.aiaa.org/doi/abs/10.2514/6.2012-540.

[40] M. Samorani, The wind farm layout optimization problem, in: Handbook of Wind Power Systems, Springer Berlin Heidelberg, Berlin, Heidelberg, 2013, pp. 21–38, http://dx.doi.org/10.1007/978-3-642-41080-2_2.

[41] D. Cazzaro, D. Pisinger, Variable neighborhood search for large offshore wind farm layout optimization, Comput. Oper. Res. 138 (2022) 105588, http://dx.doi.org/10.1016/j.cor.2021.105588.

[42] NREL, FLORIS. Version 2.2.0, 2020, URL https://github.com/NREL/floris.

[43] A. Niayifar, F. Porté-Agel, Analytical modeling of wind farms: A new approach for power prediction, Energies 9 (9) (2016) 1–13, http://dx.doi.org/10.3390/en9090741.

[44] E. Machefaux, G.C. Larsen, J.P. Leon, Engineering models for merging wakes in wind farm optimization applications, J. Phys. Conf. Ser. 625 (1) (2015) http://dx.doi.org/10.1088/1742-6596/625/1/012037.

[45] P. Virtanen, R. Gommers, T.E. Oliphant, M. Haberland, T. Reddy, D. Cournapeau, E. Burovski, P. Peterson, W. Weckesser, J. Bright, S.J. van der Walt, M. Brett, J. Wilson, K.J. Millman, N. Mayorov, A.R.J. Nelson, E. Jones, R. Kern, E. Larson, C.J. Carey, İ. Polat, Y. Feng, E.W. Moore, J. VanderPlas, D. Laxalde, J. Perktold, R. Cimrman, I. Henriksen, E.A. Quintero, C.R. Harris, A.M. Archibald, A.H. Ribeiro, F. Pedregosa, P. van Mulbregt, SciPy 1.0 Contributors, SciPy 1.0: Fundamental algorithms for scientific computing in python, Nat. Methods 17 (2020) 261–272, http://dx.doi.org/10.1038/s41592-019-0686-2.

[46] P. Ouro, L. Ramírez, M. Harrold, Analysis of array spacing on tidal stream turbine farm performance using Large-Eddy Simulation, J. Fluids Struct. 91 (2019) 102732, http://dx.doi.org/10.1016/j.jfluidstructs.2019.102732, URL https://www.sciencedirect.com/science/article/pii/S0889974619301161.